IEEE Access
Multidisciplinary | Rapid Review | Open Access Journal

Received September 6, 2019, accepted September 12, 2019,
date of publication September 16, 2019, date of current version October 4, 2019.

Digital Object Identifier 10.1109/ACCESS.2019.2941549

A Novel 4D-CT Sorting Method Based on Combined Mutual Information and Edge Gradient

JUAN YANG, XIAOKUN HU, GUANGPU SHAO, AND JIMIN YANG
School of Physics and Electronics, Shandong Normal University, Jinan 250358, China

Corresponding author: Juan Yang (juan.yang@sdnu.edu.cn)

This work was supported in part by the National Natural Science Foundation of China under Grant 61741117 and Grant 11747085, in part by the Natural Science Foundation of Shandong Province under Grant ZR2017BF008, and in part by the Postdoctoral Science Foundation of China under Grant 2016M600554.

ABSTRACT Although mutual information is a general method usually being used to measure the similarity of two images, the robustness is questionable due to the absence of spatial information. The purpose of this study is to develop a feasible sorting technique for 4D-CT. A novel sorting algorithm named mutual information and edge gradient (MIEG), which includes spatial information by combining mutual information with a term based on the edge gradient of the image, was proposed to sort sequential CT images. The edge of image was extracted by calculating the wavelet transform modulus maxima, and the gradient similarity coefficient of the edge image was calculated and used to multiply by mutual information to form the final similarity metric. This sorting technique was validated by comparing the 4D-CTs reconstructed using MIEG and Real-time Position Management system (Varian Medical Systems, Inc., Palo Alto, CA). Tumor motion trajectories derived from 4D-CTs were analyzed in three orthogonal directions. Their correlation coefficients (CC) and differences in tumor motion magnitude (Ds) were determined. In addition, Dice similarity coefficient (DSC) was used to measure how well the tumor volumes segmented from the two 4D datasets overlapped with each other. For all patients, the mean CC values were >0.95 in all directions. The mean Ds were <0.64 mm in all directions. In addition, good overlapping was achieved between the segmented volumes with the mean DSC $= 0.97$ at end- and median-inspiration phases, respectively. This study proposed a feasible sorting method for 4D-CT, and its usefulness in imaging accurate tumor motion has been demonstrated.

INDEX TERMS 4D-CT sorting, dice similarity coefficient, mutual information, similarity metric, wavelet transform modulus maxima.

I. INTRODUCTION

With the ability of imaging patient-specific breathing motion, four-dimensional computed tomography (4D-CT) has been widely used in radiation therapy to determine individual safety margins [1]–[11]. However, an appropriate respiratory surrogate is essential to simulate the internal respiratory motion for 4D-CT reconstruction. Currently, representative external surrogates such as reflective markers placed on body surface [12], elastic belts [13] and stain spirometers [14] are popularized in 4D-CT simulation. The individual respiratory signals are determined by tracking the motion trajectories of these external surrogates followed by determination of respiratory phases or amplitudes, and then the acquired two-dimensional (2D) CT images at different couch positions were retrospectively sorted according to phases or amplitudes. Images that are of the same phase or amplitude are put into the corresponding three-dimensional (3D) volume dataset that is used for the reconstruction of 4D images which could reflect the phase and amplitude information during breathing [15]–[24].

However, since the anatomic structures are complex and the breathing pattern is patient-specific, the definite relationship between the respiratory signal acquired using external surrogate and the movement of chest and abdomen has not been confirmed [25]. A study has found phase shift

The associate editor coordinating the review of this manuscript and approving it for publication was Xiao-Yu Zhang.

between the movement of the chest wall and the external marker that placed on the abdomen [26]. In addition, we have observed that the placement of the belt around the body frequently causes anatomical changes, introducing uncertainties in fusion with CT and subsequently dose calculation. Berglinge et al [27] proposed a simple 4D-CT reconstruction method based on lever principle. A fine needle placed on the body surface fluctuated with the respiratory movement of the patient, thus the acquired CT images could be resorted according to the respiratory phases by analyzing the motion trajectory of the fine needle images. However, the intermediate states of expiration or inspiration could not be recognized, and the effects introduced by the artifacts of the needle could not be neglected.

Studies that use internal or image-based surrogates to acquire breathing signals in 4D-CT were carried out. He et al [28] proposed a Bayesian model based automated 4D-CT lung image reconstruction for helical mode scans. The results indicated that the proposed algorithm yielded more accurate reconstruction and fewer artifacts in the 4D-CT image series. However, the complex nature of this technique is the major factor limiting its implementation in radiation therapy. Cai et al [29] utilized body area (BA) as a respiratory surrogate to extract breathing signals from presorted 4D-CT images. All CT images were acquired with a scanner operated in axial cine mode. The authors validated the performance of the BA as a respiratory surrogate by comparing the BA-derived phases with the RPM-derived phases. The disadvantage of this study is that a single threshold was used to determine the BA contour. However, the CT signal and noise often vary between patients and sometimes may even vary for the same patient. Using a single threshold to determine BA contour for all patients is suboptimal, which may have potential negative effect on accuracy validation. Furthermore, respiratory motion modeling is capable of performing more accurate understanding of respiratory motion's effect on dose distribution to cancers in the thorax and abdomen received radiotherapy. Zhang et al [30] developed a model of respiration-induced organ motion in the thorax without the commonly adopted assumption of repeatable breath cycles, which has potential for improving the accuracy of dose calculation in radiotherapy.

A study proposed by Li and Liu [15] showed an automatic 4D-CT sorting algorithm which required collecting the image data with a cine scan protocol. The sorting technique was based on employing normalized cross-correlation (NCC) to calculate the spatial continuity to select out images from the adjacent couch position. However, because the cross correlation was calculated by the joint histogram of two images, which mainly use the statistical characteristics of the image gray level, and doesn't take the relationship of pixels in different regions of the same level, the algorithms performed badly when the motion artifact was very obvious in CT images. Johnston et al [31] demonstrated a method of reducing motion artifacts in 4D-CT by incorporating anatomic similarity into phase or displacement based sorting protocols. The authors insisted that two slices might have a high correlation if they are anatomically similar. The 2D correlation coefficients between slices bordering the interface between adjacent couch positions were calculated for all candidate pairings. Cui et al [32] developed an automated method to objectively compare two 4D CT image sets and identify the one with the fewer or smaller artifacts. The method was based on image similarity between edge slices at adjacent couch positions, which was expressed by the NCC between these slices.

Inspired by the studies mentioned above, we developed a robust sorting technique for 4D-CT reconstruction as a supplement. To achieve both technical simplicity and sufficient image quality, a novel sorting algorithm named mutual information and edge gradient information (MIEG) method was proposed to perform on presorted 4D-CT images at adjacent couch positions. Images from the adjacent couch position were selected out according to mutual information combined with edge gradient information to improve the insufficient capacity of spatial continuity based sorting technique in sorting CT images. The accuracy of reconstructed 4D-CT for motion measurement was assessed on 15 lung cancer patients. The preliminary results indicated that this algorithm yielded more accurate reconstruction in 4D-CT image series.

II. MATERIALS AND METHODS

A. PATIENTS AND IMAGING STUDY

Fifteen patients (9 male, 6 female, age 47 $\sim$ 78 years) who had non-small cell lung cancer (NSCLC) (n = 11) or small cell lung cancer (SCLC) (n = 4) were enrolled in this study, which was approved by the Institutional Review Board of Shandong Cancer Hospital and Institute. The study was carried out using the patients' presorted 4D-CT images and the corresponding Real-time Position Management (RPM) data. These 4D-CT images were acquired on a GE sixteen-slice CT scanner (Lightspeed, GE Healthcare, Milwaukee, WI), along with the RPM system (Varian Medical Systems, Inc., Palo Alto, CA) and advantage 4D software (GE Healthcare, Milwaukee, WI). The 4D-CT scan was acquired in cine mode, in which the cine duration was set to the patient's average respiratory period plus one second to make sure that the scan time covered at least one whole respiratory cycle, and the cine time (image acquisition time per phase and per slice) was set to one-tenth of the breathing period. When the data collection at present couch was completed, the x-ray beam was automatically stopped and then the table moved to the next couch position and began the next round data collection until the last couch position. The following imaging parameters were used: 120kV, 290mA, 2.5mm slice thickness, gantry rotation of 0.5 seconds per cycle, reconstruction matrix of 512 $\times$ 512, field of view 450-500 mm. All CT scans were obtained prior to the planning CT scan as part of the routine diagnostic protocol for lung cancer. All patients were positioned head-first supine with the arms raised above the head. Vacuum bags were used to immobilize the patients during image acquisition. The 4D-CT sorted by the Advantage 4D software based

on the RPM data, denoted as 4D-CT_RPM, was used as gold-standard to validate the accuracy of our sorting technique. Table 1 summarizes the clinical characteristics of the patients.

TABLE 1. Summary of patients' clinical characteristics.

Patient	Gender	Age(y)	Cancer Site	Tumor Location	Staging
1	F	58	NSCLC	R-L Lobe	T2
2	M	78	NSCLC	L-L Lobe	T3
3	M	60	NSCLC	R-L Lobe	T2
4	F	68	NSCLC	L-U Lobe	TI
5	M	47	SCLC	R-U Lobe	T2
6	F	75	NSCLC	R-L Lobe	T3
7	M	62	SCLC	L-U Lobe	TI
8	M	58	NSCLC	L-L Lobe	T2
9	M	55	NSCLC	R-U Lobe	T3
10	M	73	NSCLC	R-L Lobe	T3
11	F	50	SCLC	L-U Lobe	TI
12	M	61	NSCLC	R-U Lobe	T2
13	M	56	NSCLC	R-L Lobe	T3
14	F	64	SCLC	L-U Lobe	TI
15	F	70	NSCLC	R-U Lobe	T2

M=male, F=female, NSCLC=non-small cell lung cancer, SCLC=small cell lung cancer, R-L=right-lower, L-L=left-lower, L-U=left upper, R-U=right-upper.

The index of the each acquired presorted 4D-CT image included three parameters: couch position p, slice location s and phase position n. The images were represented as $I_n(p, s)$ ($n \in [1, N], s \in [1, S], p \in [1, P]$). N and P indicated the total number of breathing phases and couch positions, respectively. S represented the total number of image slices at a specific couch position. Fig.1 shows the schematic of correspondence between the location of image data and the image index. The top rectangle represented the scan range of the patient. The lower diagram illustrated the index format of image data acquired from two scan couch positions from phase 1 to phase N.

B. SELECTION OF IMAGE DATA CONFINED WITHIN ONE SINGLE RESPIRATORY CYCLE

Since the scanning time for a couch position equals to the patient's respiratory cycle plus one second, the acquired 4D-CT actually involves a complete set of breathing cycle combined with repeated images at the same respiratory phases. Thus it was necessary to truncate the original data into a single breathing cycle. The image data truncation method used in this study was similar as Li's previous publication [10] and will only be briefly described here.

For a specific couch position p and slice location s, the NCC values were calculated to achieve data truncation. The NCC was defined as

$$C(p, s) = c(I_{n=1}(p, s),\ I_{n\in[1,N]}(p, s)) \tag{1}$$

where $I_{n\in[1,N]}(p, s)$ indicates the time series of images corresponding to couch position p and slice location s. $I_{n=1}(p, s)$ represents the first time series of images within $I_{n\in[1,N]}(p, s)$. The NCC value began with the value of 1, and gradually reduced to a minimum followed by increasing to a local maximum. When the values returned to a local maximum, the time series were truncated at the time point. As Fig.2 shows, for each scanning position, the NCC values between the first images at the first phase with images at other phases were calculated. The averaged NCC value of four columns was used

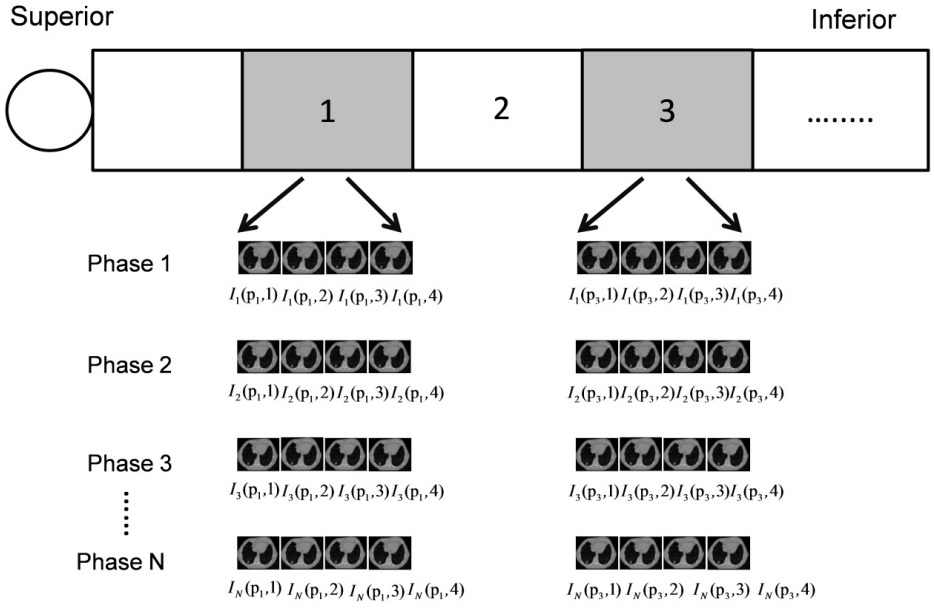

FIGURE 1. 4D-CT raw data acquisition and image index. The top rectangular represented the scanned range. The lower rectangular illustrated the specific image index form relative to two different couch positions (1 and 3) at different acquisition phases.

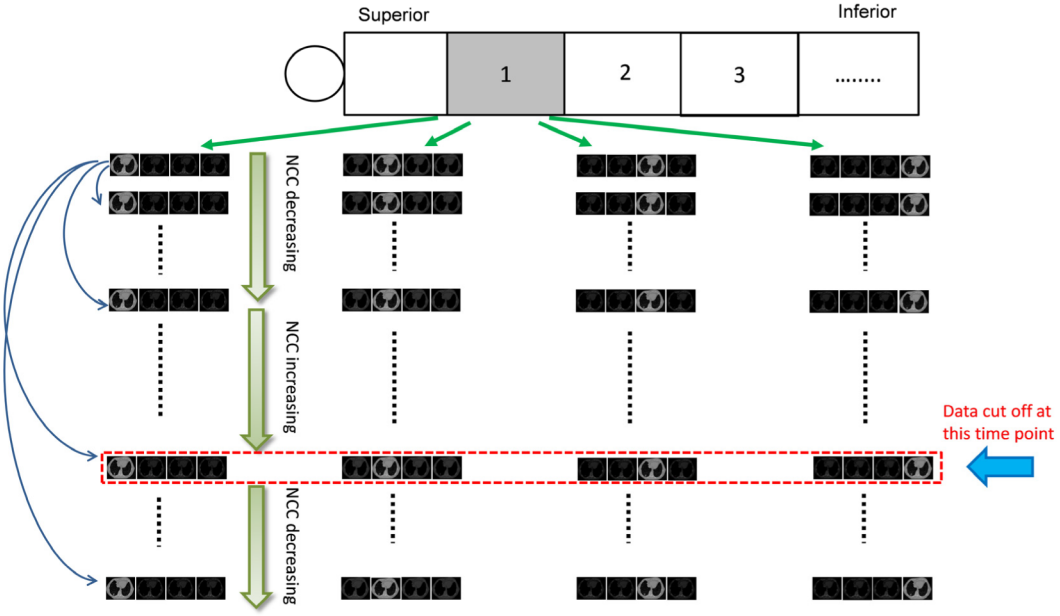

FIGURE 2. Diagram illustrates the determination of a whole respiratory cycle. The NCC values between the reference image ($I_1(p_1, s)$) and other images ($I_n(p_1, s)$, $n \in (2, N)$) at the same slice location were calculated. Since the NCC values gradually reduced to a minimum and then increased to a local maximum, the time series were cut off at the time point corresponding to the maximum NCC value.

for data truncation for each couch position. Theoretically, it may be more direct to calculate NCC for entire couch position, but NCC calculation is based on two images rather than image groups. Thus, other similarity metrics with capable of measuring similarity of two image groups are preferred. The same truncation results may be potentially obtained by using the averaged NCC and entire couch position NCC.

It is worth noting that the NCC values were not converted to breathing phases within each couch position in this study as it is common with other 4D-CT sorting techniques. Data truncation guaranteed the acquired images confined within a complete respiratory cycle. Images were classified into appropriate respiratory bins according to the novel sorting algorithm, and all the images in a bin were grouped together to form a 3D volume. Reformatted coronal views and 3D reconstruction step displayed the final 4D images. The breathing phases for each reconstructed 3D volumes were determined manually according to anatomic changes (for example, with 0% corresponding to end-of-inhalation and 50% corresponding to end-of-exhalation) or by using software.

C. SORTING TECHNIQUE BASED ON MIEG METHOD

The purpose of sorting procedure is to select the images with the same respiratory phase from all couch positions after multiple cine scanning, followed by allocating them into image volume corresponding to phase bin. After breathing cycle truncation, the next step was to use the complete cyclic image sequences to sort images. The contour changes between adjacent image slices at the same phase were continuous, since the scanned patient had anatomic continuity. Thus it can be concluded that the contours of adjacent image slices were the most similar.

In this study from the first couch position, regarding the first time series of images as sorting reference, image sequences of the second couch were sorted in accordance with the phase order of the first couch based on the characteristic of spatial continuity. Then the second couch position was taken as the new reference position to sort the images of the third couch position until the images of the last couch position were sorted. Once two certain images from two adjacent couch positions were determined at the same phase, other images at adjacent couch position could be directly assigned according to the phases of images at the previous couch due to spatial continuity.

1) IMAGE SIMILARITY BASED ON MUTUAL INFORMATION (MI)

The MI is a popularized metric to measure the similarity between two images. And it is defined as:

$$I(A, B) = H(A) + H(B) - H(A, B) \tag{2}$$

where $I(A, B)$ represents MI value between A and B. $H(A)$ and $H(B)$ indicate entropies of A and B, respectively. $H(A, B)$ is the joint entropy of A and B. The more similar of two images, the larger value the MI is. However, respiratory movement of the irradiated patient usually blurs acquired images, which potentially changes the pixel values of the images resulting in influencing the MI calculation. Thus it might be inadequate to adopt the individual MI serving as the

metric of similarity and continuity. A preferred strategy may incorporate a complementary metric for determining spatial continuity of images with artifacts.

2) EDGE DETECTION BY CALCULATING WAVELET MODULUS MAXIMA

Currently, many image edge detection approaches have been proposed which include gradient operator, laplace operator, Robert operator, and wavelet analysis. The proposed previous methods are not satisfactory in anti-noise performance and edge localization due to the high-frequency signals of both. However, the multi-resolution feature of wavelet transformation proposes a novel method for edge detection. It is appropriate for extracting local feature and has the ability of achieving noise suppression while extracting image edges.

Mallat and Hwang [33] proposed an approach of using wavelet transformation modulus local maxima to detect image edge. It is supposed that $\Psi(x, y)$ represents a 2D smooth function, and it could be regarded as an impulse response of a low-pass filter. $\Psi^1(x, y)$ and $\Psi^2(x, y)$ indicate the first and second partial derivatives of $\Psi(x, y)$ in x and y directions, respectively. They are defined as following:

$$\Psi^1(x, y) = \partial\Psi(x, y)/\partial x \tag{3}$$
$$\Psi^2(x, y) = \partial\Psi(x, y)/\partial y \tag{4}$$

where $\Psi^1(x, y)$ and $\Psi^2(x, y)$ can be used as basic wavelet functions, and in each scale they are defined as follows:

$$\Psi^1_{2^j}(x, y) = \frac{1}{4^j}\Psi^1(\frac{x}{2^j}, \frac{y}{2^j}) \tag{5}$$
$$\Psi^2_{2^j}(x, y) = \frac{1}{4^j}\Psi^2(\frac{x}{2^j}, \frac{y}{2^j}) \tag{6}$$

There is a corresponding energy function $f(x, y)$ in each scale of 2^j, and the 2D wave transformation of $f(x, y) \in L^2(R^2)$ can be decomposed as two independent directions as:

$$W^1_{2^j}f(x, y) = f\Psi^1_{2^j}(x, y) \tag{7}$$
$$W^2_{2^j}f(x, y) = f\Psi^2_{2^j}(x, y) \tag{8}$$

where $W^1_{2^j}f(x, y)$ and $W^2_{2^j}f(x, y)$ represent the gradients of $f(x, y)$ smoothed by $\Psi(x, y)$ on the scale of 2^j in x and y directions, respectively. The wavelet transform vector was defined as following:

$$W_{2^j}f(x, y) = \begin{bmatrix} W^1_{2^j}f(x, y) \\ W^2_{2^j}f(x, y) \end{bmatrix} \tag{9}$$

And the magnitude $M_{2^j}f(x, y)$ and argument $A_{2^j}f(x, y)$ of the gradient were calculated as

$$M_{2^j}f(x, y) = \sqrt{\left|W^1_{2^j}f(x, y)\right|^2 + \left|W^2_{2^j}f(x, y)\right|^2} \tag{10}$$

$$A_{2^j}f(x, y) = Arg[W_{2^j}f(x, y)] = tan^{-1}\left[\frac{W^2_{2^j}f(x, y)}{W^1_{2^j}f(x, y)}\right] \tag{11}$$

The argument reflects the direction of the gradient at the scale of 2^j. The edges are defined as the locations where $M_{2^j}f(x, y)$ equals to the extremum values, and its direction is along the vertical direction of $A_{2^j}f(x, y)$. The complete edge image was obtained by fusing all edges detected at different scales.

3) COMPARISON OF GRADIENT SIMILARITY

The gradient of each pixel in image is generally described by direction and magnitude. The point x in image A is supposed to be corresponding with x' in image B. The gradient can be used to represent the maximum value and direction of grayscale drop at x and x', and the angle between the gradient vectors can be described as:

$$\alpha_{AB} = arccos\frac{\nabla x \nabla x'}{|\nabla x|\,|\nabla x'|} \tag{12}$$

where ∇x and $\nabla x'$ represent the gradients of x and x' in image A and B, respectively. $|\nabla x|$ and $\left|\nabla x'\right|$ are the corresponding gradient magnitudes. For the same anatomic position, the gradient directions of corresponding pixels in edge images are mostly the same or opposite. In order to well detect this similarity, the gradient similarity measure is defined as:

$$w(\alpha) = \frac{cos(2\alpha) + 1}{2} \tag{13}$$

The gradient similarity measure equals to 1 when two images are well matched with each other. The complete gradient similarity measure between two images is defined as:

$$G(A, B) = \sum_{(x,x')\in(A\cap B)} w(\alpha_{x,x'})min(|\nabla x|, \left|\nabla x'\right|) \tag{14}$$

The similarity value can reach to a maximum when the spatial information of two images is exactly the same.

4) THE SIMILARITY MEASUREMENT COMBINED MUTUAL INFORMATION WITH EDGE GRADIENT

For two images A and B, the wavelet transformation modulus maxima method was used to detect the edges. And the edge gradient similarity $EG(A, B)$ was calculated by equation (14). The novel similarity measurement named MIEG was defined as the edge gradient similarity $EG(A, B)$ multiplied by the calculated mutual information $MI(A, B)$ between two images.

$$MIEG(A, B) = EG(A, B) \times MI(A, B) \tag{15}$$

Based on spatial continuity, the contour changes of two spatially adjacent scanning sections were continuous between each other. For two adjacent couches, the cross-correlation of the adjacent scanning sections which were in the same respiratory phase was the closest. The time series of images corresponding to the same couch position and slice generate a complete periodic image sequence which changes continuously in time. In order to find a set of optimal sorting results, this algorithm proposed a cyclic sorting to the whole series of images. Between the last column of the reference couch position and the first column of the registered couch position to be sorted, the cyclic sorting method was adopted to calculate the similarity of each sorting method. Then a set of optimal solutions could be found as the best way to sort the images.

After cyclic sorting on two adjacent couches, a similarity matrix could be obtained as

$$C_g(m) = C(I_n(p, S), I_i(p + 1, 1)) \tag{16}$$

where $n \in [1, N]$, $i \in [1, N]$, and $m \in [1, M]$. The operator $C(\cdot)$ represents the calculation of MIEG values between two image series. After cyclic sorting, $C_g(m)$ was actually a $M \times M$ matrix, of which $M = N$, because each column of $C_g(m)$ represented a similarity of one sorting method. m was only used as the parameter of index. The optimal sorting method was

$$G_{optim} = min(sum(\left|C_g(m) - \overline{C_r}\right|)) \tag{17}$$

where $\overline{C_r}$ was the average value of the similarity at the reference couch position:

$$\overline{C_r} = Average(C_r(1), C_r(2) \ldots C_r(S - 1)) \tag{18}$$

$C_r(i)$, $(i \in [1, S - 1])$ indicates the calculated MIEG values between slice i and slice $i+1$ at the reference couch position. It is worth noting that $C_r(i)$ is a matrix with the size of $1 \times N$. Thus the best way to sort the couches to be sorted was identified. Then the optimal sorting method was regarded as new reference sorting method, and the next couch was seen as new couch to be sorted. The searching process of optimal sorting method was repeatedly run in this way until the last one couch was sorted. An in-house developed software was used to combine image contour and spatial continuity for binning raw 4D-CT images affected by artifacts.

D. RECONSTRCUTION OF 4D-CT

After the image sorting using the novel technique, images at different couch positions with the same phase were put into a corresponding phase bin. The contour changes of images in the same phase bin were the most continuous. All the images in each phase formulated a 3D dataset which was a necessity for 4D image reconstructing. The 4D-CT dataset was reconstructed by reconstructing and arranging these 3D datasets with different respiratory phases.

E. COMPARISON OF 4D- TUMOR TRAJECTORIES

Tumor motion trajectories in three orthogonal directions (superior-inferior (SI), anterior-posterior (AP) and medial-lateral (ML)) derived from the reconstructed 4D-CT using MI, EG, Advantage 4D software and MIEG method were obtained using an automatic cross-correlation tracking algorithm based on NCC. Tumor motion tracking using this algorithm has been used in previous literatures [34], [35]. Tumor trajectories in the SI and AP directions were acquired through tracking the sagittal CT images, and tumor trajectories in the ML direction were extracted through tracking the coronal CT images. Although the SI tumor motion information can also be obtained from coronal CT images, we did not use that information because the through-plane (i.e., AP) tumor motion in coronal plane could not be neglected. For sagittal CT images, the through-plane (i.e., ML) tumor motion is of less concern since tumor motion in the ML direction is typically very small (<2 mm). The templates were drawn manually as a matrix box in the lung tumor in 4D-CTs. To minimize tracking errors due to human variation in template selection, the tracking was repeated five times. Although our intention was to use the same template in each tracking process, the base template was drawn manually and could be slightly different between different tracking processes. Using repeated measurements to determine the average tumor and diaphragm motion trajectories can reduce this human variation.

Tumor motion trajectories determined from 4D-CT_RPM, 4D-CT_MI, 4D-CT_EG and 4D-CT_MIEG were compared. Specifically, correlation coefficient (CC) and the difference in motion magnitude between the motion trajectories were calculated for each patient. The difference in motion magnitude was calculated as the mean difference in motion magnitude over the total respiratory phases. In addition, tumor volumes in 4D-CT_MIEG and 4D-CT_RPM were segmented and compared. Dice similarity coefficient (DSC) was used to measure how well the tumor volumes in the two 4D datasets overlapped with each other.

In addition, our proposed sorting technique was further compared with two currently existing approaches used for 4D-CT reconstruction: image boundary discontinuity-based (IBD) method [36] and BA method [29]. Tumor motion trajectories determined from 4D-CT_IBD, 4D-CT_BA and 4D-CT_MIEG were analyzed for all patients with the 4D-CT_RPM used as the golden standard. The correlation coefficient and the difference in motion magnitude between the motion trajectories were calculated.

III. RESULTS

Results of 4D-CT reconstruction on a total of 15 clinically acquired sequential CT images from lung cancer patients were reported. The image data was collected by a physician who was not familiar with image processing techniques, only on the basis of image collection without any screening criteria.

Fig.3 shows the results of NCC values calculated between the first image series and other sequential image series at the first couch position. The four curves represent the calculated results of the four column images. It was obvious that the values began with the value of 1, and then gradually reduced to a minimum followed by increasing to a local maximum. Thus the image series were truncated at the time point with the maximum NCC value to obtain a complete breathing period, which indicated Phase 10 this figure.

Fig.4 shows an example of 4D-CT reconstruction results. The coronal and sagittal images were reconstructed using the proposed MIEG sorting method. The dash lines facilitated the visualization of respiratory motion of the lung tumor.

Fig.5 shows the comparison of tumor motion trajectories between 4D-CT_RPM, 4D-CT_MI, 4D-CT_EG and 4D- CT_MIEG for a representative patient. Ten respiratory phases were involved in 4D-CTs reconstructed using different

TABLE 2. Summary of patients' clinical characteristics comparison of CC and D values between tumor motion trajectories derived from 4D-CT_RPM, 4D-CT_MI, 4D-CT_EG and 4D-CT_MIEG.

Patient	4D-CT$_{RPM}$ vs 4D-CT$_{MIEG}$						4D-CT$_{RPM}$ vs 4D-CT$_{MI}$						4D-CT$_{RPM}$ vs 4D-CT$_{EG}$						DSI	
	CC			D (mm)			CC			D (mm)			CC			D (mm)				
	SI	AP	ML	SI	AP	ML	SI	AP	ML	SI	AP	ML	SI	AP	ML	SI	AP	ML	EI	MI
1	0.98	0.98	0.95	0.71	0.32	0.15	0.92	0.90	0.89	1.28	1.00	0.30	0.88	0.86	0.85	1.20	1.12	0.32	0.98	0.99
2	0.99	0.97	0.96	0.78	0.42	0.20	0.93	0.94	0.88	1.00	1.36	0.26	0.80	0.84	0.70	2.06	1.18	0.49	0.96	0.97
3	0.96	0.98	0.96	0.63	0.50	0.30	0.90	0.84	0.90	1.40	1.26	0.60	0.76	0.80	0.82	1.58	1.22	0.41	0.98	0.98
4	0.98	0.96	0.96	0.55	0.28	0.10	0.88	0.90	0.80	1.20	1.16	0.28	0.76	0.70	0.74	1.69	2.04	0.37	0.95	0.96
5	0.97	0.95	0.94	0.60	0.42	0.20	0.91	0.92	0.85	1.30	1.26	0.40	0.78	0.84	0.82	1.38	1.02	0.34	0.96	0.96
6	0.89	0.92	0.90	0.74	0.40	0.35	0.90	0.84	0.90	1.24	1.50	0.60	0.88	0.85	0.76	1.40	1.26	0.43	0.97	0.98
7	0.96	0.96	0.95	0.58	0.25	0.08	0.84	0.90	0.86	1.26	1.05	0.37	0.85	0.83	0.78	1.26	1.26	0.38	0.94	0.95
8	0.95	0.92	0.96	0.60	0.35	0.10	0.92	0.93	0.84	1.40	1.20	0.36	0.89	0.83	0.90	1.24	1.20	0.40	0.98	0.98
9	0.96	0.98	0.97	0.68	0.35	0.10	0.94	0.92	0.90	1.22	1.04	0.26	0.90	0.88	0.86	1.10	2.01	0.35	0.99	0.96
10	0.98	0.96	0.95	0.49	0.38	0.26	0.90	0.92	0.92	1.26	1.20	0.26	0.90	0.88	0.89	1.05	1.14	0.35	0.95	0.97
11	0.97	0.98	0.94	0.60	0.32	0.12	0.92	0.93	0.88	1.22	1.20	0.50	0.82	0.85	0.80	1.40	1.36	0.36	0.99	0.98
12	0.96	0.94	0.95	0.64	0.42	0.18	0.89	0.89	0.84	1.32	1.20	0.36	0.80	0.85	0.82	1.38	1.32	0.40	0.92	0.96
13	0.95	0.96	0.93	0.72	0.40	0.24	0.88	0.91	0.87	1.30	1.10	0.40	0.82	0.80	0.84	1.42	1.38	0.38	0.99	0.98
14	0.98	0.97	0.97	0.56	0.34	0.20	0.90	0.90	0.90	1.20	1.10	0.21	0.83	0.82	0.78	1.36	1.35	0.30	0.98	0.97
15	0.94	0.95	0.96	0.68	0.37	0.16	0.91	0.87	0.86	1.26	1.00	0.35	0.91	0.83	0.81	1.44	1.34	0.46	0.95	0.96
Mean	0.96	0.96	0.95	0.64	0.37	0.18	0.90	0.90	0.87	1.26	1.20	0.37	0.84	0.83	0.81	1.40	1.35	0.38	0.97	0.97
SD	0.03	0.02	0.02	0.09	0.07	0.09	0.02	0.03	0.04	0.11	0.15	0.13	0.06	0.05	0.07	0.31	0.37	0.05	0.02	0.01

SI=superior-inferior, AP=anterior-posterior, ML=medial-lateral, CC=correlation coefficient, D=difference on motion magnitude, DSI=dice similarity index, EI=end-inspiration, MI=middle-inspiration, SD=standard deviation.

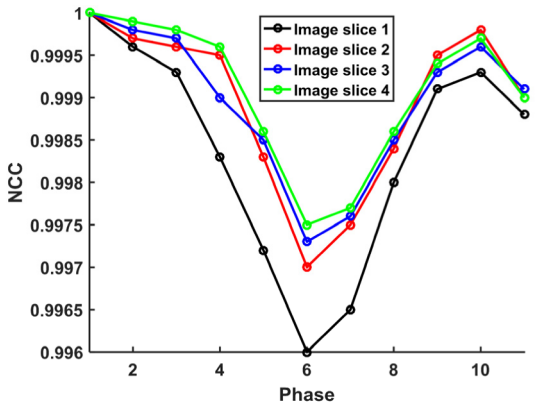

FIGURE 3. The cross-correlation values calculated between the first image series and other image series at the first couch position. The four curves indicate four image slices.

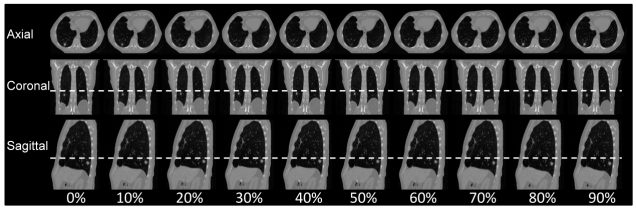

FIGURE 4. An example of 4D-CT reconstruction result at 10 respiratory phases. The coronal and sagittal plane images were reconstructed based on our proposed method. The dash lines facilitated the visualization of respiratory motion of the lung tumor.

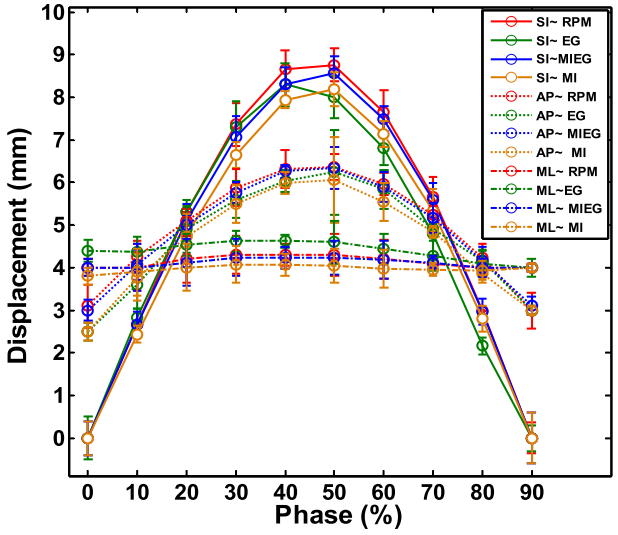

FIGURE 5. Comparison of the motion trajectories determined from the 4D-CT_MIEG, 4D-CT_RPM, 4D-CT_EG, and 4D-CT_MI of a representative case.

sorting method. Error bars are standard deviations of multiple measurements. Good matching was observed between 4D-CT_RPM and 4D-CT_MIEG: the CC ranged from 0.95 to 0.98, and the mean difference of motion magnitude ranged from 0.15 mm to 0.71 mm, with the largest difference in the SI direction. Suboptimal matching was observed between 4D-CT_RPM, 4D-CT_MI and 4D-CT_EG. For 4D-CT_RPM and 4D-CT_MI, the CC ranged from 0.89 to 0.92, and the mean difference of motion magnitude ranged from 0.30 mm to 1.28 mm. For 4D-CT_RPM and 4D-CT_EG, the CC ranged from 0.85 to 0.88, and the mean difference of motion magnitude ranged from 0.32 mm to 1.20 mm.

Table 2 summarizes the results of all patients. On average, the tumor motion trajectories matched well between

4D-CT_RPM and 4D-CT_MIEG: the means of CC were 0.96 ± 0.03, 0.96 ± 0.02, and 0.95 ± 0.02 in the SI, AP and ML directions, respectively. The mean Ds were 0.64 ± 0.09, 0.37 ± 0.07, and 0.18 ± 0.09 in the SI, AP and ML directions, respectively. Suboptimal matching was observed between 4D-CT_RPM, 4D-CT_MI and 4D-CT_EG. For 4D-CT_RPM and 4D-CT_MI, the CC were 0.90 ± 0.02, 0.90 ± 0.03, and 0.87 ± 0.04 in the SI, AP and ML directions, respectively. And the mean Ds were 1.26 ± 0.11, 1.20 ± 0.15, and 0.37 ± 0.13 in the SI, AP and ML directions, respectively. For 4D-CT_RPM and 4D-CT_EG, the CC were 0.84 ± 0.06, 0.83 ± 0.05, and 0.81 ± 0.07 in the SI, AP and ML directions, respectively. And the mean Ds were 1.40 ± 0.31, 1.35 ± 0.37, and 0.38 ± 0.05 in the SI, AP and ML directions, respectively. In addition, good overlapping was achieved between the segmented volumes of 4D-CT_RPM and 4D-CT_MIEG: at end-inspiration phase, mean DSC = 0.97 ± 0.01; while at median-inspiration phase, mean DSC = 0.97 ± 0.02.

In addition, Fig.6 demonstrated the comparison of tumor motion trajectories between 4D-CT_RPM, 4D-CT_MIEG, 4D-CT_IBD and 4D-BA for a representative patient. Good matching was observed between 4D-CT_RPM and 4D-CT_MIEG: the CC ranged from 0.95 to 0.98, and the mean difference of motion magnitude ranged from 0.15 mm to 0.71 mm, with the largest difference in the SI direction. Suboptimal matching was observed between 4D-CT_RPM, 4D-CT_IBD and 4D-CT_BA. For 4D-CT_RPM and 4D-CT_IBD, the CC ranged from 0.75 to 0.94, and the mean difference of motion magnitude ranged from 0.20 mm to 0.95 mm. For 4D-CT_RPM and 4D-CT_BA, the CC ranged from 0.80 to 0.96, and the mean difference of motion magnitude ranged from 0.12 mm to 0.76 mm.

For all patients, suboptimal matching was observed between 4D-CT_RPM, 4D-CT_IBD and 4D-CT_BA compared with the results between 4D-CT_RPM and 4D-CT_MIEG shown in Table 3. For 4D-CT_RPM and 4D-CT_IBD, the CC were 0.90 ± 0.06, 0.86 ± 0.04, and 0.82 ± 0.02 in the SI, AP and ML directions, respectively. And the mean Ds were 0.70 ± 0.02, 0.50 ± 0.04, and 0.22 ± 0.03 in the SI, AP and ML directions, respectively. For 4D-CT_RPM and 4D-CT_BA, the CC were 0.92 ± 0.05, 0.92 ± 0.03, and 0.92 ± 0.03 in the SI, AP and ML directions, respectively. And the mean Ds were 0.71 ± 0.08, 0.50 ± 0.09, and 0.42 ± 0.11 in the SI, AP and ML directions, respectively.

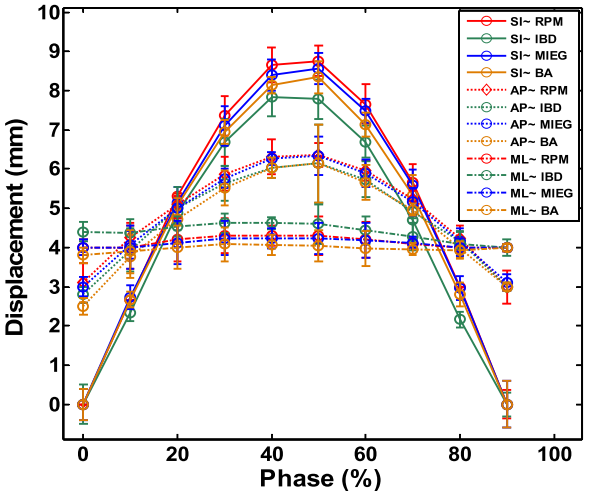

5

FIGURE 6. Comparison of the motion trajectories determined from the 4D-CT_MIEG, 4D-CT_RPM, 4D-CT_IBD, and 4D-CT_BA of a representative case.

Currently, the commercialized 4D-CT reconstruction system usually utilizes RPM device to monitor the displacements of the body surface's movement or measures the expiratory volume using the spirometer, and then sorts the CT images according to respiratory phases. However, the respiratory signals transferred from body surface's movement are not synchronized with inside organs, and the value of spirometer needs to be corrected since it has shifts along with time (E and GT). Fig. 7 shows the comparison of image artifacts in 4D-CTs reconstructed using RPM method and MIEG method at phase 20%, 40% and 60%. The artifacts indicated by the arrows were severe in 4D-CT_RPM, but largely reduced in 4D-CT_MIEG.

In this study, we gave a whole comparison between our proposed sorting method and common method in clinic or approaches presented in recent literatures. After validation of 15 lung cancer patients' image data, observations showed that the breathing motion of 4D-CT reconstructed using MIEG was comparable with 4D-CT reconstructed with RPM, and the apparent motion artifacts were reduced. The movement condition and the moving region of the tumor and the organ in each phase of the respiratory cycle could be seen. The proposed method outperformed these methods in most

TABLE 3. Summary of patients' clinical characteristics comparison of CC and D values between tumor motion trajectories derived from 4D-CT_RPM, 4D-CT_MIEG, 4D-CT_IBD and 4D-CT_BA.

	4D-CT$_{RPM}$ vs 4D-CT$_{MIEG}$						4D-CT$_{RPM}$ vs 4D-CT$_{IBD}$						4D-CT$_{RPM}$ vs 4D-CT$_{BA}$					
	CC			D(mm)			CC			D(mm)			CC			D(mm)		
Value	SI	AP	ML	SI	AP	ML	SI	AP	ML	SI	AP	ML	SI	AP	ML	SI	AP	ML
Range	0.89-0.99	0.92-0.98	0.90-0.97	0.49-0.78	0.25-0.50	0.10-0.35	0.75-0.94	0.82-0.90	0.80-0.93	0.55-0.95	0.38-0.60	0.20-0.58	0.90-0.94	0.86-0.95	0.80-0.96	0.50-0.76	0.30-0.60	0.12-0.40
Middle	0.94	0.95	0.93	0.60	0.35	0.24	0.82	0.86	0.90	0.78	0.46	0.30	0.92	0.93	0.90	0.68	0.49	0.36
Mean	0.96	0.96	0.95	0.64	0.37	0.18	0.90	0.86	0.89	0.70	0.50	0.22	0.92	0.90	0.92	0.71	0.50	0.42
SD	0.03	0.02	0.02	0.09	0.07	0.09	0.06	0.04	0.02	0.02	0.04	0.03	0.05	0.04	0.03	0.08	0.09	0.11

SI=superior-inferior, AP=anterior-posterior, ML=medial-lateral, CC=correlation coefficient, D=difference on motion magnitude, SD=standard deviation.

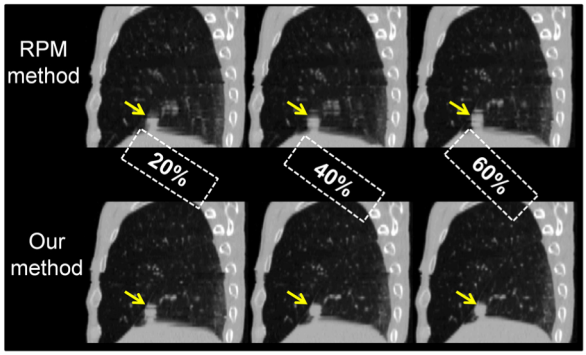

FIGURE 7. An example of 4D-CT reconstruction result at 10 respiratory phases. The coronal and sagittal plane images were reconstructed based on our proposed method. The dash lines facilitated the visualization of respiratory motion of the lung tumor.

cases by considering the results of measured CC and difference in motion magnitude. That illustrated the feasibility of 4D-CT image sorting algorithm based on MIEG method.

IV. DISCUSSION

In this study, we evaluated the feasibility of a novel sorting technique based on the calculation of MI and the detection of surface contour to reconstruct 4D-CT in 15 patients with lung cancer. Preliminary results demonstrated that the reconstructed 4D-CT had comparable motion accuracy with the gold-standard. It was unnecessary to collect the respiratory signals synchronized with the CT images, which overcame the limitation of using external respiratory monitor devices to reconstruct 4D-CT. In addition, the sorting method was established independently without having any relationship with the software of CT machine, with the ability of being appropriate for clinical radiation therapy.

In the study by Chen and colleagues [10], the authors proposed a sorting method using spatial continuity, which was convinced that for two adjacent couches the cross-correlation of the cross-sections which were in the same respiratory phase and spatially continuous were the closet. The NCC was used as a metric for image similarity to confine the image data into a single respiratory cycle as we did in this study. However, no extra auxiliary behavior was employed to compensate the drawbacks of the NCC method, since it selected the images at the same respiratory phase from adjacent couch positions by calculating the correlation of gray level of pixels in two images. Thus it may be a suboptimal method by only using the NCC as a metric to measure the similarity and continuity of images when motion artifacts appear. In this study the edge of image were extracted by calculating the wavelet transform modulus maxima, and the gradient similarity coefficients of edge image was calculated, since the surface body contours of adjacent images in spatial dimension at the same respiratory phase may be the most similar. Image edge detection must meet the conditions of performing effective noise suppression and accurate edge detection.

Although this new approach is an improvement over Li's study, a limitation of this study lies in the combination of spatial continuity and contour information. A product of these two individual similarity measurements was utilized to solve the problem of sorting images with artifacts in this study. However, patients suffered pulmonary cancers have independent respiratory motion, and the motion artifacts in acquired images are significantly different. It might be more sensible to implement adaptive proportion of the two measurements according to different patients. Furthermore, an automatic parameter setting may be preferred to make the programming more applicable. In addition, tumors in other locations have distinct motion patterns compared with tumors in pulmonary. Thus, appropriate sorting parameters for other cancers are still needed to explore, and a systematized adaptive sorting technique for 4D-CT reconstruction is the final goal.

Another limitation of this study is that the wavelet transform modulus maxima was calculated to aid evaluate the contour similarity and it may be suboptimal for small lesions, since the edge detected can be overshadowed by other anatomical structures. However, contour detection was performed for the whole image rather than the lesion. The detected contours of small lesions may have relatively little effect on the similarity calculation. Otherwise, adaptive sorting parameters can be applied for different locations of the image according to artifacts. A large weight may be given to the calculated MI value for small lesions affected by artifacts. In addition, artifacts were observed in some 4D-CT images. The 4D-CT volume images exhibited ''gaps'' at multiple locations and at multiple respiratory phases. These artifacts were presumably caused by patient respiratory variations, as commonly observed in 4D-CT images. The 4D techniques (both CT and MRI) acquire images at each slice location intermittently, rather than continuously during whole breathing cycles. Thus, the collection of an image at every slice position in every respiratory phase is not guaranteed, resulting in the ''gaps''.

A final limitation is that this pilot study included a limited number of patients and assessed only patients with pulmonary cancers. Since this is a feasibility study, it did not include large amounts of patient data, but focused on methodology presentation and feasibility validation. A larger pool of patients is needed in future studies in order to answer the following questions: (1) Is this sorting method effective to cancers in other locations treated by radiotherapy, such as liver cancer? (2) Are there any other better methods to demonstrate the accuracy of respiratory motion in reconstructed 4D-CT? (3) How does irregular respiration affect the accuracy of tumor motion measurement of 4D-CT?

V. CONCLUSION

We have successfully proposed and evaluated a sorting algorithm combing similarity calculation and contour detection to reconstruct 4D-CT in patients with lung cancer(s). Preliminary results demonstrated that the reconstructed 4D-CT sorted by MIEG method showed comparable motion accuracy as the RPM method. However, the evaluation and comparison in the current study was limited by its small

sample size. A larger follow-up study has a better chance of quantifying the reliability of our results.

REFERENCES

[1] J. Yang, D. Li, Y. Yin, F. Zhao, and H. Wang, "Evaluation of demons- and FEM-based registration algorithms for lung cancer," *Technol. Cancer Res. Treat.*, vol. 15, pp. 275–284, Apr. 2016.

[2] P. Keall, "4-dimensional computed tomography imaging and treatment planning," *Seminars Radiat. Oncol.*, vol. 14, no. 1, pp. 81–90, 2004.

[3] D. A. Low, M. Nystrom, E. Kalinin, P. Parikh, J. F. Dempsey, J. D. Bradley, S. Mutic, S. H. Wahab, T. Islam, G. Christensen, D. G. Politte, and B. R. Whiting, "A method for the reconstruction of four-dimensional synchronized CT scans acquired during free breathing," *Med. Phys.*, vol. 30, pp. 1254–1263, Jun. 2003.

[4] G. S. Mageras, A. Pevsner, E. D. Yorke, K. E. Rosenzweig, E. C. Ford, A. Hertanto, S. M. Larson, D. M. Lovelock, Y. E. Erd, S. A. Nehmeh, J. L. Humm, and C. C. Ling, "Measurement of lung tumor motion using respiration-correlated CT," *Int. J. Radiat. Oncol. Biol. Phys.*, vol. 60, pp. 933–941, Nov. 2004.

[5] T. Pan, "Comparison of helical and cine acquisitions for 4D-CT imaging with multislice CT," *Med. Phys.*, vol. 32, pp. 627–634, Feb. 2005.

[6] E. Rietzel, T. Pan, and G. T. Chen, "Four-dimensional computed tomography: Image formation and clinical protocol," *Med. Phys.*, vol. 32, pp. 874–889, Apr. 2005.

[7] J. Girija, G. N. K. Murthy, and P. C. Reddy, "4D medical image registration: A survey," in *Proc. Int. Conf. Intell. Sustain. Syst. (ICISS)*, Dec. 2017, pp. 539–547.

[8] M. Lambrecht, J.-J. Sonke, U. Nestle, H. Peulen, D. C. Weber, M. Verheij, and C. W. Hurkmans, "Quality assurance of four-dimensional computed tomography in a multicentre trial of stereotactic body radiotherapy of centrally located lung tumours," *Phys. Imag. Radiat. Oncol.*, vol. 8, pp. 57–62, Oct. 2018.

[9] E. Steiner, C.-C. Shieh, V. Caillet, J. Booth, R. O'Brien, A. Briggs, N. Hardcastle, D. Jayamanne, K. Szymura, T. Eade, and P. Keall, "Both four-dimensional computed tomography and four-dimensional cone beam computed tomography under-predict lung target motion during radiotherapy," *Radiotherapy Oncol.*, vol. 135, pp. 65–73, Jun. 2019.

[10] L. Thomas, T. Schultz, V. Prokic, M. Guckenberger, S. Tanadini-Lang, M. Hohberg, M. Wild, A. Drzezga, and R. A. Bundschuh, "4D-CT-based motion correction of PET images using 3D iterative deconvolution," *Oncotarget*, vol. 10, pp. 2987–2995, Apr. 2019.

[11] R. Werner, T. Sentker, F. Madesta, T. Gauer, and C. Hofmann, "Intelligent 4D CT sequence scanning (i4DCT)," *Int. J. Radiat. Oncol. Biol. Phys.*, vol. 102, p. S5, Nov. 2018.

[12] P. J. Keall, G. Starkschall, H. Shukla, K. M. Forster, V. Ortiz, C. W. Stevens, S. S. Vedam, R. George, T. Guerrero, and R. Mohan, "Acquiring 4D thoracic CT scans using a multislice helical method," *Phys. Med. Biol.*, vol. 49, pp. 2053–2067, May 2004.

[13] T. Kleshneva, J. Muzik, and M. Alber, "An algorithm for automatic determination of the respiratory phases in four-dimensional computed tomography," *Phys. Med. Biol.*, vol. 51, pp. N269–N276, Jul. 2006.

[14] T. Pan, T.-Y. Lee, E. Rietzel, and G. T. Y. Chen, "4D-CT imaging of a volume influenced by respiratory motion on multi-slice CT," *Med. Phys.*, vol. 31, pp. 333–340, Feb. 2004.

[15] C. Li and J. Liu, "An algorithm for 4D CT image sorting using spatial continuity," *J. X-Ray Sci. Technol.*, vol. 21, no. 3, pp. 323–333, 2013.

[16] N. Wink, C. Panknin, and T. D. Solberg, "Phase versus amplitude sorting of 4D-CT data," *J. Appl. Clin. Med. Phys.*, vol. 7, no. 1, pp. 77–85, 2006.

[17] C. Zhao, Y. Zhong, J. Wang, and M. Jin, "Modified simultaneous motion estimation and image reconstruction (m-SMEIR) for 4D-CBCT," in *Proc. IEEE 15th Int. Symp. Biomed. Imag. (ISBI)*, Apr. 2018, pp. 340–343.

[18] S. Sauppe, J. Kuhm, M. Brehm, P. Paysan, D. Seghers, and M. Kachelrieß, "Motion vector field phase-to-amplitude resampling for 4D motion-compensated cone-beam CT," *Phys. Med. Biol.*, vol. 63, Feb. 2018, Art. no. 035032.

[19] D. Lee, S. Kim, J. Palta, B. Lewis, P. Keall, and T. Kim, "A retrospective 4D-MRI based on 2D diaphragm profiles for lung cancer patients," *J. Med. Imag. Radiat. Oncol.*, vol. 63, pp. 360–369, Jun. 2019.

[20] T. Mitsumoto, R. Minamimoto, F. Sunaoka, S. Kishimoto, K. Inoue, and M. Fukushi, "The clinical utility of phase-based respiratory gated PET imaging based on visual feedback with a head-mounted display system," *Brit. Inst. Radiol.*, vol. 92, Jun. 2019, Art. no. 20180233.

[21] Z. van Kesteren, A. van der Horst, O. J. Gurney-Champion, I. Bones, D. Tekelenburg, T. Alderliesten, G. van Tienhoven, R. Klaassen, H. W. M. van Laarhoven, and A. Bel, "A novel amplitude binning strategy to handle irregular breathing during 4DMRI acquisition: Improved imaging for radiotherapy purposes," *Radiat. Oncol.*, vol. 14, May 2019, Art. no. 80.

[22] X.-Y. Zhang, S. Wang, and X. Yun, "Bidirectional active learning: A two-way exploration into unlabeled and labeled data set," *IEEE Trans. Neural Netw. Learn. Syst.*, vol. 26, no. 12, pp. 3034–3044, Dec. 2015.

[23] X.-Y. Zhang, S. Wang, X. Zhu, X. Yun, G. Wu, and Y. Wang, "Update vs. upgrade: Modeling with indeterminate multi-class active learning," *Neurocomputing*, vol. 162, pp. 163–170, 2015/08/25/ 2015.

[24] X.-Y. Zhang, H. Shi, X. Zhu, and P. Li, "Active semi-supervised learning based on self-expressive correlation with generative adversarial networks," *Neurocomputing*, vol. 345, pp. 103–113, Jun. 2019.

[25] R. Li, J. H. Lewis, L. I. Cerviño, and S. B. Jiang, "4D CT sorting based on patient internal anatomy," *Phys. Med. Biol.*, vol. 54, pp. 4821–4833, Aug. 2009.

[26] G. Carnes, S. Gaede, E. Yu, J. Van Dyk, J. Battista, and T.-Y. Lee, "A fully automated non-external marker 4D-CT sorting algorithm using a serial cine scanning protocol," *Phys. Med. Biol.*, vol. 54, pp. 2049–2066, Apr. 2009.

[27] K. Berlinger, O. Sauer, L. Vences, and M. Roth, "A simple method for labeling CT images with respiratory states," *Med. Phys.*, vol. 33, no. 9, pp. 3144–3148, Sep. 2006.

[28] T. He, Z. Xue, B. S. Teh, and S. T. Wong, "Reconstruction of four-dimensional computed tomography lung images by applying spatial and temporal anatomical constraints using a Bayesian model," *J. Med. Imag.*, vol. 2, Apr. 2015, Art. no. 024004.

[29] J. Cai, Z. Chang, Z. Wang, W. P. Segars, and F.-F. Yin, "Four-dimensional magnetic resonance imaging (4D-MRI) using image-based respiratory surrogate: A feasibility study," *Med. Phys.*, vol. 38, pp. 6384–6394, Dec. 2011.

[30] Q. Zhang, A. Pevsner, A. Hertanto, Y.-C. Hu, K. E. Rosenzweig, C. C. Ling, and G. S. Mageras, "A patient-specific respiratory model of anatomical motion for radiation treatment planning," *Med. Phys.*, vol. 34, pp. 4772–4781, Dec. 2007.

[31] E. Johnston, M. Diehn, J. D. Murphy, B. W. Loo, Jr., and P. G. Maxim, "Reducing 4D CT artifacts using optimized sorting based on anatomic similaritya)," *Med. Phys.*, vol. 38, pp. 2424–2429, May 2011.

[32] G. Cui, B. Jew, J. C. Hong, E. W. Johnston, B. W. Loo, Jr., and P. G. Maxim, "An automated method for comparing motion artifacts in cine four-dimensional computed tomography images," *J. Appl. Clin. Med. Phys.*, vol. 13, no. 6, pp. 170–180, Nov. 2012.

[33] S. Mallat and W. L. Hwang, "Singularity detection and processing with wavelets," *IEEE Trans. Inf. Theory*, vol. 38, no. 2, pp. 617–643, Mar. 1992.

[34] J. Yang, J. Cai, H. Wang, Z. Chang, B. G. Czito, M. R. Bashir, and F.-F. Yin, "Four-dimensional magnetic resonance imaging using axial body area as respiratory surrogate: Initial patient results," *Int. J. Radiat. Oncol. Biol. Phys.*, vol. 88, pp. 907–912, Mar. 2014.

[35] J. Yang, J. Cai, H. Wang, Z. Chang, B. G. Czito, M. R. Bashir, M. Palta, and F.-F. Yin, "Is diaphragm motion a good surrogate for liver tumor motion?" *Int. J. Radiat. Oncol. Biol. Phys.*, vol. 90, pp. 952–958, Nov. 2014.

[36] K. Yuan, C. Duan, and Z. Tian, "A 4D CT sorting algorithm based on image boundary discontinuity," in *Proc. Int. Conf. Med. Image Anal. Clin. Appl.*, Jun. 2010, pp. 147–150.

JUAN YANG was born in Linyi, China, in 1985. She received the B.S. and M.S. degrees in signal processing from Shandong Normal University, in 2011, and the Ph.D. degree in medical physics from Shandong University, Jinan, in 2015. From September 2012 to September 2014, she was a joint Ph.D. Student with Duke University, USA, sponsored by the China Scholarship Council.

Since 2015, she has been a Lecturer with the School of Physics and Electronics, Shandong Normal University. She is the author of more than 10 articles. She has given many oral presentations at AAPM meetings. Her research interests include medical image registration, 4D image reconstruction, and image segmentation based on deep learning.

XIAOKUN HU was born in Linyi, China, in 1994. She received the B.S. degree in electronic information engineering from Shandong Normal University, in 2017, where she is currently pursuing the master's degree with the School of Physics and Electronics. Her research interests include medical image registration and 4D image reconstruction.

GUANGPU SHAO was born in Heze, China, in 1994. He received the B.S. degree in electronic information engineering from Shandong Normal University, in 2017, where he is currently pursuing the master's degree in signal and information processing with the School of Physics and Electronics. His research interests include medical image registration, 4D image reconstruction, and image segmentation based on deep learning.

JIMIN YANG was born in Jinan, China, in 1961. He received the B.S. degree from the School of Information Science and Engineering, Shandong University, China, in 1982. From 1982 to 1988, he was a Lecturer with Nanjing Tech University. Since 1988, he has been a Professor with the School of Physics and Electronics, Shandong Normal University. He is the author of two books, more than 50 articles, and more than 10 inventions. His research interests include design of embedded systems, digital signal processors, and research and development of medical instruments.